Insect pectinate antennae maximize odor capture efficiency at intermediate flight speeds

Mourad Jaffar-Bandjee[a,b], Thomas Steinmann[a], Gijs Krijnen[b], and Jérôme Casas[a,1]

[a]Institut de Recherche sur la Biologie de l'Insecte, UMR 7261, CNRS, Université de Tours, 37200 Tours, France; and [b]Robotics and Mechatronics, University of Twente, 7500 AE Enschede, The Netherlands

Edited by James H. Tumlinson, Pennsylvania State University, University Park, PA, and approved September 30, 2020 (received for review May 12, 2020)

Flying insects are known to orient themselves over large distances using minute amounts of odors. Some bear pectinate antennae of remarkable architecture thought to improve olfactory performance. The semiporous, multiscale nature of these antennae influences how odor molecules reach their surface. We focus here on the repeating structural building blocks of these antennae in Saturniid moths. This microstructure consists of one ramus or branch and its many hair-like sensilla, responsible for chemical detection. We experimentally determined leakiness, defined as the proportion of air going through the microstructure rather than flowing around it, by particle image velocimetry visualization of the flow around three-dimensional printed scaled-up mock-ups. The combination of these results with a model of mass transfer showed that most pheromone molecules are deflected around the microstructure at low flow velocities, keeping them out of reach. Capture is thus determined by leakiness. By contrast, at high velocities, molecular diffusion is too slow to be effective, and the molecules pass through the structure without being captured. The sensory structure displays maximal odor capture efficiency at intermediate flow speeds, as encountered by the animal during flight. These findings also provide a rationale for the previously described "olfactory lens," an increase in pheromone reception at the proximal end of the sensors. We posit that it is based on passive mass transfer rather than on physicochemical surface processes.

olfaction | fluid dynamics | mass transfer | pheromone | pectinate antenna

Insects make use of olfaction for many tasks, such as searching for food, suitable habitats and sexual partners (1). One of the most spectacular examples is the use of sexual pheromones in the Lepidoptera (2). In many moth species, the females release tiny amounts of sex pheromone to attract male conspecifics (3). These pheromones can travel over relatively long distances, up to several hundred meters (4). At such a distance, detecting the very low concentrations of pheromone present is a challenge. Some moth species, including Saturniid moths in particular, have developed pectinate antennae (5), which have a very complex shape. Saturniid moths cannot feed as adults (6, 7). Consequently, the adults survive for only a few days, during which they must find a mating partner. It is thought that their pectinate antennae are optimized for the sole role of olfaction, to facilitate the detection of sex pheromones.

Moth olfaction can be divided into several steps. First, the antenna captures the pheromone molecules present in the air. These molecules then reach the chemical detectors located in the sensilla. The information delivered is then processed by the neural system, inducing a particular behavior (8). Here, we focus exclusively on the first step, the capture of pheromone molecules by the antenna, because this is the step during which antenna shape can influence olfactory performance. Pheromones are captured when they enter olfactory pores. These small apertures allow the pheromone molecules to get into the tubules for capture by the odor-binding proteins in the hemolymph (9). They are evenly distributed over the surface of the sensilla (10). The surface area of the sensilla can therefore be used as a proxy for the number of pores.

Furthermore, the velocity of the air close to the sensilla is influenced by the shape of the entire antenna. An antenna can increase its capture efficiency in two ways. Firstly, capture efficiency can be increased by increasing the area of contact between the antenna and the air. This area increases with the size and number of sensilla. Secondly, capture efficiency can be increased by modifying airflow past the antenna as follows. The antenna can be seen as a permeable object. Air can either flow through the structure of the antennae or can be deflected around the whole antenna. In the second case, the molecules carried by the air are not available to the sensilla. The proportion of air passing through the antennae tends to decrease with their resistance to air, with an increasing number of sensilla, for example.

In this study, we investigated the effects of pectinate antenna shape on the capture of molecules through alterations to the air velocity field around sensilla. We focused on antenna geometry, determining its efficiency in terms of the proportion of molecules captured as a function of the incoming pheromone mass flux. We explored a large range of relative velocities between the air and the antenna, to cover the full range of wind velocities and flight speeds (0.5 $m \cdot s^{-1}$ to 3 $m \cdot s^{-1}$) experienced by the animal.

For practical reasons, we limited our study to a single species, *Samia cynthia*. We first describe the shape of its antenna. The antennae of this species can be considered to have three levels

Significance

Some insects, especially moths, bear pectinate antennae, elaborate organs generally used to detect low concentrations of pheromone released by potential sexual partners. The shape of these antennae is crucial for efficient pheromone detection, as it influences airflow and, thus, pheromone capture. Pectinate antennae are highly complex. We therefore focused our study on a subunit of the antenna: a single branch of the antenna and the sensory hairs it carries. We found that the geometry of this subunit was most efficient at moth flight velocities, allowing enough air to flow through it and enough time for diffusion to ensure the capture of pheromone molecules. Our findings have implications for porous microarray sensors, such as those based on microcantilevers.

Author contributions: M.J.-B., G.K., and J.C. designed research; M.J.-B. and T.S. performed research; M.J.-B., T.S., G.K., and J.C. analyzed data; and M.J.-B., T.S., G.K., and J.C. wrote the paper.

The authors declare no competing interest.

This article is a PNAS Direct Submission.

Published under the PNAS license.

[1]To whom correspondence may be addressed. Email: jerome.casas@univ-tours.fr.

This article contains supporting information online at https://www.pnas.org/lookup/suppl/doi:10.1073/pnas.2007871117/-/DCSupplemental.

Downloaded at UNIVERSITEIT TWENTE on November 5, 2020

ECOLOGY

ENGINEERING

(Fig. 1 *A* and *B*): the flagellum or main branch, the rami (secondary branches perpendicular to the flagellum), and the sensilla. The sensilla are mostly located on the rami. There is a difference of four orders of magnitude in size between the diameter of the sensilla (∼3 μm) and the total length of the antenna (∼1 cm). This complex multiscale geometry made it difficult to investigate a complete antenna (11, 12). Indeed, the geometry of an antenna, where boundary conditions have to be defined, is difficult to describe in an analytical formula or requires a huge number of elements in a numerical simulation. In an experimental approach, building such complex objects is still a challenge, even with the help of three-dimensional (3D) printing (13). We therefore split the antenna into two levels of organization: the flagellum plus the rami, and a single ramus plus its sensilla. We focus here exclusively on the second of these levels of organization, which we refer to hereafter as the microstructure, because the sensilla host the chemical detectors. One of the key parameters considered is the upstream orientation of the sensilla, longitudinal to the airflow.

Two aspects of the architecture of the microstructure are particularly important and complicate attempts to determine capture efficiency: the geometry of the antenna and its leakiness, due to its finite dimensions (14). We dealt with these two aspects separately. The microstructure has an intricate shape, with sensilla located on each ramus (Fig. 1*B*). We modeled a simplified microstructure with a 2D array of longitudinal cylinders with diameters and lengths comparable to those of the sensilla. We adapted an analytical formula developed by Miyatake and Iwashita (15) for heat transfer to measure mass transfer between a fluid and an infinite array of horizontal cylinders. The microstructure is also a finite permeable structure. In many studies, permeable structures are located within tubes (16, 17), so all fluid particles must pass through these structures. Only a few studies have tackled the case of permeable structures in an open flow field: Air partly flows through and is partly deflected around the whole structure (11, 18). We evaluated the proportion of airflow passing between the sensilla and carrying the molecules potentially able to reach their surface, by performing particle image velocimetry (PIV) on a large-scale 3D printed artificial microstructure. As proposed by Cheer and Koehl (19), we call this proportion the "leakiness" of the microstructure. This leakiness provides a measurement of the airflow between sensilla and, thus, also of the mean air velocity between sensilla. This velocity is particularly important, as it defines the air velocity used as an input in the model of mass transfer described above (Fig. 2).

In summary, our approach involved investigation of the geometry of the microstructure of the moth antenna (Fig. 1*B*), followed by the development of a model of mass transfer based on a simplified geometry (Fig. 1*C*), and the production of a scaled-up 3D printed microstructure for the evaluation of leakiness by PIV (Fig. 1*D*). Finally, we combined the results of the previous two sections to calculate the capture efficiency of the microstructure (Fig. 2).

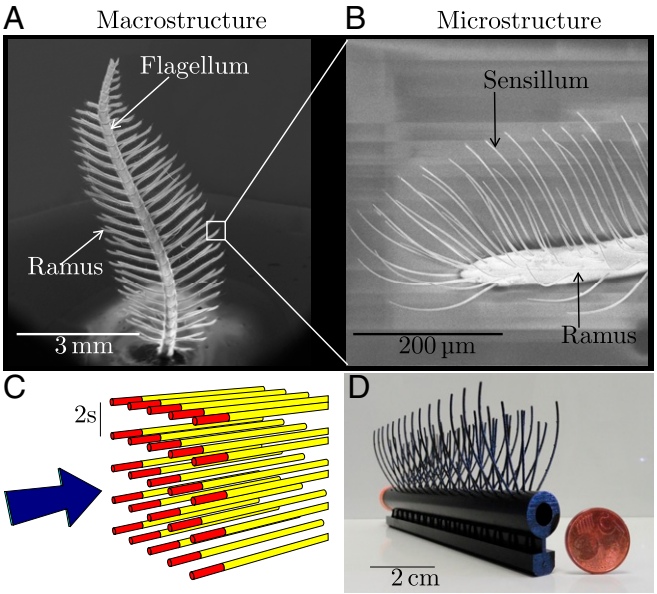

Fig. 1. Geometries of the natural and artificial antennae. (*A*) Scanning electron micrograph of the macrostructure, consisting of the flagellum and rami. (*B*) Magnification of the tip of a ramus, revealing the sensilla. (*C*) Array of semiinfinite cylinders. The cylinders are arranged in a square array of side 2*s*. The direction of airflow is indicated by the arrow: The cylinders face the flow. The number of cylinders is infinite in the direction orthogonal to the direction of the flow. The local mass transfer coefficient is determined assuming semiinfinite cylinders, but the total mass transfer is integrated only on the red portion (from the tip to the length of the sensillum). (*D*) The 3D printed microstructure used for leakiness assessments in the PIV experiments.

Results

We first present the relative capture rates of pheromones predicted by the model, followed by the experimental estimation of leakiness. By combining the two, we can calculate capture efficiency, a relative measure. We then focus on the presence of a spatially restricted region at the tip of the sensilla at which capture is enhanced, confirming the presence of a previously observed "olfactory lens."

Pheromone Capture Efficiency Decreases with Increasing Flow Speed. By adapting the work of Miyatake and Iwashita (15), we determined the local mass transfer $F_{\mathrm{cyl}}(z)$ on a slice of cylinder of length $\mathrm{d}z$ depending on the local coefficient of mass transfer $K_M(z)$,

$$F_{\mathrm{cyl}}(z) = K_M(z)\pi d_0\,(c_{\mathrm{f}}(z) - c_{\mathrm{cyl}})\,\mathrm{d}z. \quad [1]$$

Local mass transfer $F_{\mathrm{cyl}}(z)$ depends on the local pheromone concentration in the fluid $c_{\mathrm{f}}(z)$, pheromone concentration at the surface of the sensillum c_{cyl}, and the local coefficient of mass transfer $K_M(z)$. The local concentration $c_{\mathrm{f}}(z)$ varies along the sensillum but is averaged within the fluid, in a direction perpendicular to the sensillum. The local coefficient of mass transfer can be obtained by using the local value of the Sherwood number $\mathrm{Sh}_{\mathrm{loc}}(z)$, analogous to the Nusselt number (*SI Appendix*).

As air flows along the sensilla, it is depleted of its molecules, accounting for the dependence on concentration c_{f} with z. Using a suitable mass balance on a slice of fluid around a sensillum, we can determine $c_{\mathrm{f}}(z)$, as described in Fig. 4, *Inset*,

$$F_{\mathrm{in}}(z) - F_{\mathrm{out}}(z) = F_{\mathrm{cyl}}(z), \quad [2]$$

with

$$F_{\mathrm{in}}(z) = w_{\mathrm{mod}}\,c_{\mathrm{f}}(z) \quad [3]$$

$$F_{\mathrm{out}}(z) = w_{\mathrm{mod}}\,c_{\mathrm{f}}(z + \mathrm{d}z), \quad [4]$$

and $w_{\mathrm{mod}} = 4s^2$ is the volume flux per cylinder in a square array of side $2s$ (Fig. 1*C*). Thus

$$w_{\mathrm{mod}}\,c_{\mathrm{f}}(z) - w_{\mathrm{mod}}\,c_{\mathrm{f}}(z + \mathrm{d}z) = K_M(z)\pi d_0 \mathrm{d}z\,(c_{\mathrm{f}}(z) - c_{\mathrm{cyl}}). \quad [5]$$

Hence, the variation of the fluid pheromone concentration along a cylinder is given by

Downloaded at UNIVERSITEIT TWENTE on November 5, 2020

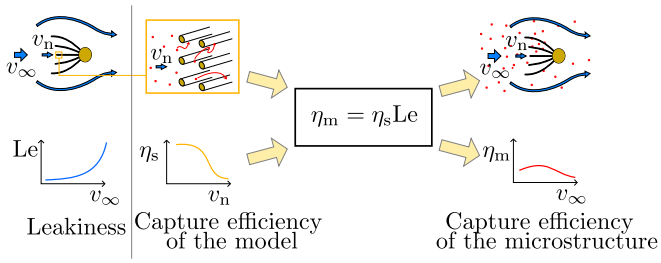

Fig. 2. Combination of model and experiments to obtain the capture efficiency of the microstructure, η_m. v_∞ is the far-field velocity, v_n is the velocity used as an input in the model, Le is the leakiness, and η_s is the capture efficiency of the model.

$$-w_{\mathrm{mod}}\frac{\mathrm{d}c_{\mathrm{f}}}{\mathrm{d}z} = K_M(z)\pi d_0\left(c_{\mathrm{f}}(z) - c_{\mathrm{cyl}}\right). \quad [6]$$

The total mass flux F_s from the fluid to the sensillum is obtained by solving Eq. **6** and by integrating the local mass flux along a cylinder with a length equal to that of a sensillum L_s.

$$F_s = \int_0^{L_s} F_{\mathrm{cyl}}(z)\mathrm{d}z. \quad [7]$$

As we modeled an infinite array of cylinders, we were able to focus on a single "average" sensillum and interchangeably use its capture rate for that of the entire array. We used a system of Eqs. **1** and **6** (Matlab R2015b 8.6.0.267246) and obtained the mass flux for a single sensillum F_s with Eq. **7**. We then calculated the capture efficiency η_s of the sensillum by dividing the previously determined mass flux F_s by the reference mass flux $F_{\mathrm{ref}}^{\mathrm{mod}}$. The reference mass flux is the volume flow rate per sensillum defined in the model multiplied by the far-field concentration,

$$F_{\mathrm{ref}}^{\mathrm{mod}} = w_{\mathrm{mod}}\, c_\infty. \quad [8]$$

The capture efficiency of the model, or, equivalently, of a single sensillum, is a relative measure, which becomes

$$\eta_s = \frac{F_s}{F_{\mathrm{ref}}^{\mathrm{mod}}}. \quad [9]$$

The capture efficiency of the model η_s decreases monotonically with increasing velocity (Fig. 4, yellow line and *SI Appendix*).

Leakiness Increases with Increasing Flow Speed. We will now consider the whole microstructure, so the variables are dependent on the far-field flow velocity v_∞. PIV experiments provided us with the velocity fields around the microstructure at several far-field velocities. Indeed, leakiness varies with far-field velocity (20, 21), so we measured it over a wide range of velocities. We then extracted leakiness by integrating the velocity field entering the microstructure and dividing it by the far-field flux for an equal area (Fig. 3 and see Table 2). Leakiness Le increased monotonically with far-field velocity (Fig. 4, blue triangles). The marked decrease observed at 0.1 $\mathrm{m{\cdot}s^{-1}}$ occurred for the artificial microstructure but also for other structures with various geometries (21). The most likely explanation for this decrease is irregularities of the motorized axis at this velocity. We used leakiness as a direct link between v_n and v_∞ (Eq. **14**) to substitute variables and express η_s as a function of v_∞ (*SI Appendix*).

Large Range of Flow Velocities with Maximal Pheromone Capture. The efficiency of the microstructure, η_m, the product of the two curves (Eq. **18** and leakiness; Fig. 2), reaches a flat maximum at about 0.5 $\mathrm{m{\cdot}s^{-1}}$ (Fig. 4, solid red line). The mass flux is limited by both the leakiness of the structure and the capture efficiency of the model. At low velocities, leakiness is the limiting factor, as most of the air flows around the structure. The remaining air flows slowly between sensilla, allowing the pheromone molecules sufficient time to diffuse to the surface of the sensilla. At higher velocities, mass capture is limited due to the array of sensilla, which is not sufficiently efficient to capture a large portion of the molecules, which pass by too rapidly. The transition between the two regimes occurs at about 0.2 $\mathrm{m{\cdot}s^{-1}}$.

Explanation for the Existence of the "Olfactory Lens." The spatial distribution of molecule capture shows a decrease along the sensilla (Fig. 5*A*). Over most of the length of the sensillum, the boundary layer is constrained by the fluid dynamic interactions of each sensillum with its neighbors, and remains constant. The boundary layer is smallest at the very tip of the sensillum, increasing down the length of the sensillum. The air is depleted of its pheromone molecules as it flows along the sensillum. As a consequence, mass transfer is more efficient at the tip, leading to a strong decrease in capture along the length of the sensillum. By spatially integrating these local capture rates, F_{cyl} (Eq. **1**), we can assess the relative importance of each half of a sensillum in pheromone capture (Fig. 5*B*). The distal half of a sensillum always captures more molecules than the proximal half. This effect is particularly pronounced at low flow velocities, due to the depletion effect. This result is independent of the value of the far-field concentration, as the mass transport equation (Eq. **10**) is linear with respect to pheromone concentration c.

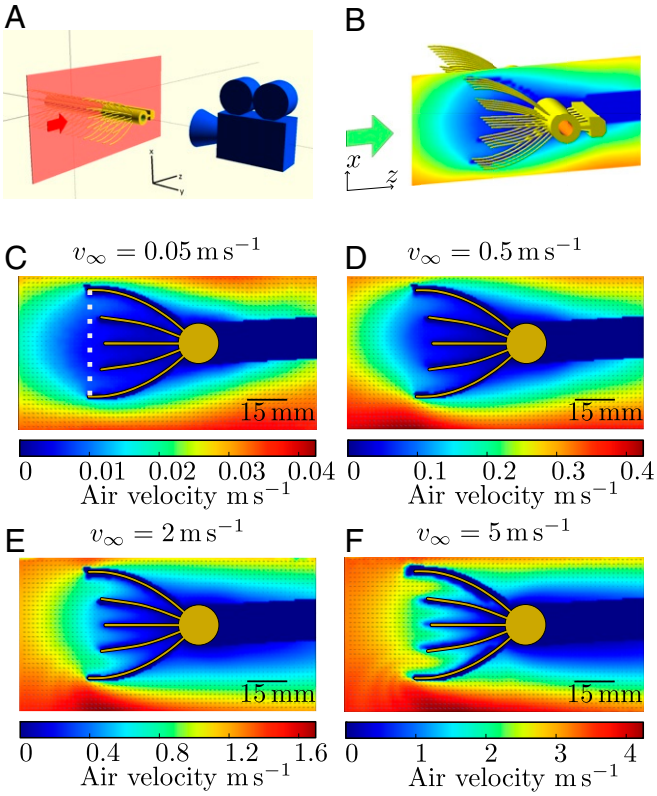

Fig. 3. PIV experiments. (*A*) Experimental setup. (*B*) Velocity field relative to the microstructure. (*C–F*) Velocity field for far-field velocities v_∞ of $\{0.05, 0.5, 2, 5\}\mathrm{m{\cdot}s^{-1}}$. The white dotted line in *C* indicates the point at which the flux used was measured for the determination of leakiness. For the sake of clarity, we indicate the line only in *C*, but it was located at the same position for the other velocities.

ECOLOGY

ENGINEERING

Downloaded at UNIVERSITEIT TWENTE on November 5, 2020

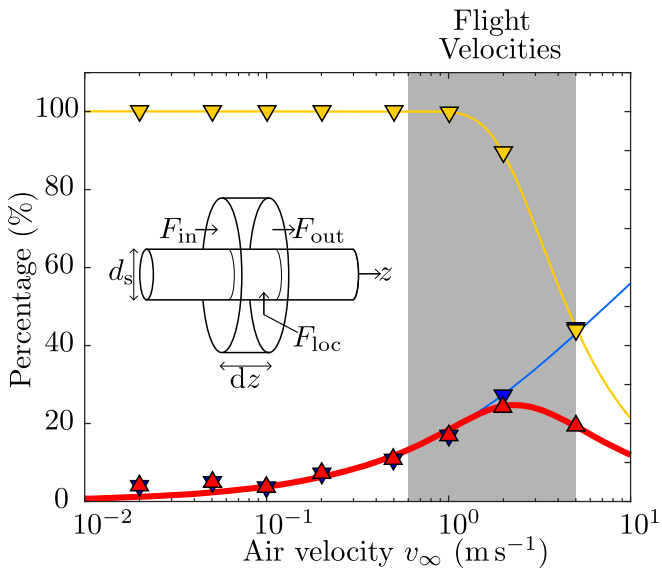

Fig. 4. Capture rate of the microstructure (red triangles), calculated as a combination of leakiness (blue triangles) and model capture rate (yellow triangle). The blue curve is an exponential fit to leakiness, with the equation $\mathrm{Le} = 32.4\exp(0.352\ln v_\infty)$. The yellow and red curves are fits to the model capture efficiency and the capture efficiency of the microstructure obtained from fitted leakiness, respectively. *Inset* shows the control volume used to determine the mass flux on a sensillum. Air flows in the direction of increasing z. F_{in} is the mass flux entering the control volume, F_{out} is the mass flux leaving the control volume, F_{loc} is the mass flux reaching the surface of the sensillum, and d_s is the diameter of a sensillum.

Discussion

Assumptions of the Model. In this study, we made a number of assumptions regarding the printed microstructure, the fluid dynamic experiments, and the model. In *SI Appendix*, we discuss these assumptions.

The Capture Efficiency Is the Result of a Trade-off. The captured pheromone flux monotonically increases with respect to the air velocity (*SI Appendix*). Thus, the faster a moth flies, the more it captures. However, drag increases with the square of the velocity at high Reynolds numbers, leading to an energy vs. capture trade-off. This might be part of the explanation why one does not see insects flying with monstrous antennae. Similar arguments are used to explain the limits imposed on other exaggerated sexual traits (22, 23). Furthermore, the monotonically increase of absolute capture flux observed for steady-state flux might be deceptive: A toy model of a finite pheromone puff shows that, in this case, the microstructure total capture is proportional to efficiency (*SI Appendix*). Thinking in terms of capture efficiency therefore enables us to identify both the physical phenomena limiting capture and the velocity range at which the microstructure is the most effective.

The capture performance of a microstructure depends on various features, the two most important being its finite dimensions and particular geometry (24). We argue that low levels of leakiness decrease the air velocity in the vicinity of sensilla, allowing more time for the pheromone molecules to be trapped by the surface of the sensilla via diffusion alone. The finite dimensions of the microstructure therefore have a crucial impact on capture performance through leakiness. Capture efficiency is furthermore modified by the specific geometric arrangement of the sensilla, the second key feature. The model of mass transfer in an infinite array of semiinfinite longitudinal cylinders facing the airflow captures the essence of this geometric problem (15). According to our model, the capture efficiency of a microstructure is the product of its leakiness and the efficiency of the infinite model. This result is in accordance with Kanaujia and Kaissling (14) where leakiness is called 'transmissivity" and efficiency of the model is called "adsorptivity." As leakiness and efficiency of the infinite model are both defined as ratios ranging between 0 and 1, their product also lies between 0 and 1 and, more importantly, is always inferior to each term. Thus, for a given air velocity, the efficiency of the microstructure is majored by their smallest values. We found that leakiness was very low at low velocity, at which it was the limiting factor, whereas a larger proportion of the air passed between the sensilla at high velocities (Fig. 4). However, at these high velocities, only a small proportion of the pheromone molecules had sufficient time to diffuse to the sensilla. We conclude that an efficient microstructure should have both a high leakiness and a small distance between sensilla. The first of these conditions implies a decrease in the number of sensilla. The second requires an increase in the number of sensilla. We thus observed a trade-off between these two limiting conditions, implying an efficiency optimum at intermediate values of air velocity. This trade-off between leakiness and capture efficiency can be understood in terms of advection and diffusion. At low velocity, advection through the antenna is the limiting factor, whereas, at high velocities, the time required for diffusion is too long for most of the molecules to reach the sensilla (*SI Appendix*).

Implications for Moth Behavior and Antenna Geometry. As observed in previous studies (25–27), the position of the sensilla relative to the supporting structure varies considerably between

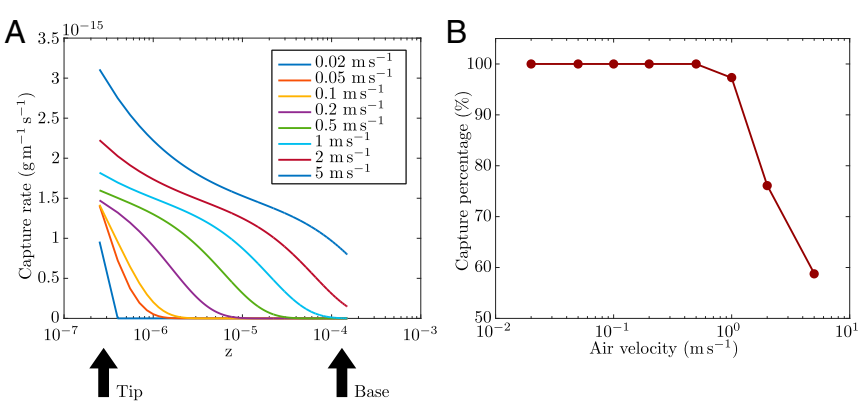

Fig. 5. The olfactory lens mechanism. (*A*) Change in mass flux F_{loc} captured along a sensillum for a far-field concentration c_∞ of 1 g·m^{-3} at various air velocities. (*B*) Relative importance of the first half of the sensillum.

Downloaded at UNIVERSITEIT TWENTE on November 5, 2020

species, with every possible combination found in nature. In this moth species and in *Bombyx mori*, the sensilla face the flow. This is surprising as, for a similar length, a cylinder positioned transverse to the flow captures molecules more efficiently than a longitudinal horizontal tube, as confirmed by our findings (*SI Appendix*). We have two explanations for the surprising geometry of the antenna in this species. First, a microstructure with transverse sensilla is probably less leaky than one with longitudinal sensilla. Thus, without greatly decreasing the leakiness of the whole microstructure, longitudinal sensilla may considerably increase the contact area. Second, as recently shown by Waldrop et al. (24), sensors located ahead of the supporting structure can extract more information, as other locations are quickly entrapped in the wake produced by the larger sustaining structures, such as the rami and the flagellum.

We found that the efficiency of the microstructure investigated was maximal at far-field velocities of 0.5 $m{\cdot}s^{-1}$ to 3 $m{\cdot}s^{-1}$, close to the flight velocities of Saturniid moths (28, 29) (more references in *SI Appendix*). This good match between our expectations and reality is tempered by the fact that we studied flow through only a portion of antenna, a single ramus and its sensilla. A real antenna has about 50 rami and fluid dynamic interactions between them would be expected, as shown by previous studies measuring the leakiness of whole antennae (20, 30). In this case, we would expect the same limiting effects of both leakiness at low velocities and pheromone capture at higher velocities to apply. However, a decrease in leakiness and a shift of the maximum efficiency to even higher, but still realistic, velocities can be expected for a complete antenna. Indeed, for a small increase of sensilla density, both leakiness and capture efficiency curves are shifted to higher values, so that we can reasonably expect the maximal efficiency to shift to higher values too. By symmetry, sparser structures should have their maxima at lower velocities (Fig. 6). The density of sensilla is thus a critical parameter and it appears that the microstructure might be designed to be the most efficient at flight velocities.

Conclusion

Our main contribution, relative to published studies on this topic (11, 12, 31), lies in our attention to the detailed geometry of the microstructure of an antenna, the geometry studied here being much closer to that found in nature than previous models (32). The few other cases where scales and orientation to the flow have been considered (33, 34) have shown that they matter for defining the capture rate, even if the antennal architecture was as simple as a cylinder. This attention to the particular features of antenna geometry, however, had its costs. Focusing on one particular geometry decreases the extent to which the results can be generalized to the diversity of antenna shapes found in nature. The focus on geometric aspects also forced us to use a steady-state model of incoming flow and concentration, precluding the characterization of temporal patterns of pheromone puffs (12, 35) which are generated by atmospheric turbulence (36) and are useful for male moths to locate female emitters (37).

Our modeling of antenna geometry and mass transfer provided us with insight into the phenomenon of the "olfactory lens" (14, 38–40). Firstly, air is depleted of its pheromone molecules as it flows along the sensilla, such that pheromone concentration is maximal at the tip of the sensilla. Secondly, the fluid boundary layer is thinnest at the outward-oriented tip, and gradually increases down the length of the sensillum. Thus, the time taken for a molecule to cross this layer increases with distance downstream from the tip. These two reinforcing mechanisms, dependent solely on antenna geometry, are sufficient to explain the "olfactory lens," first described by Kanaujia and Kaissling (14) and supported by morphological evidence showing a pore density null at the base of a sensillum, and increasing toward the tip of it (10). They found that between 60% and 70% of the pheromone are located on the distal half of the sensilla, which is in accordance with our results at observed flight velocities. It has been suggested that as yet undisclosed surface physicochemical processes are responsible for the enrichment of odors at the tip

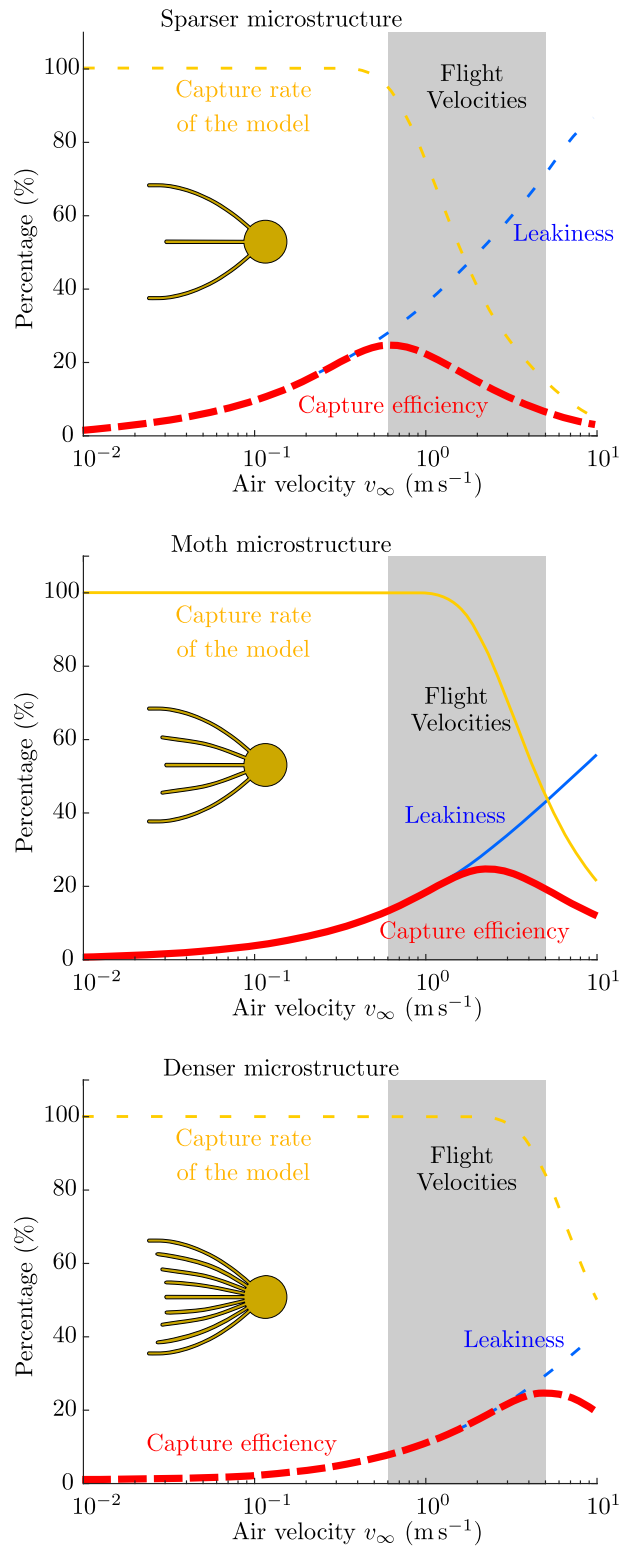

Fig. 6. Location of the maximal odor capture efficiency as function of sensilla density, from sparse (*Top*) to dense (*Bottom*) antennal architecture.

ECOLOGY
ENGINEERING

Downloaded at UNIVERSITEIT TWENTE on November 5, 2020

of the sensors (40). We provide an alternative rational explanation for this "olfactory lens" mechanism based on the processes described above.

The intricacies of flow dynamics with complex geometries preclude broad conclusions about pheromone capture efficiency. The tremendous variety of antenna forms and orientation of sensors observed in insects (41) may be understood by a combination of experiments with 3D printed mock-ups and modeling of transport phenomena, as reported here, when applied to particular types of antenna geometries. This applies equally to the microcantilever based gas sensors (see ref. 42 for a review and ref. 43 for a specific case). In all cases, the hydrodynamical interactions between the cantilevers within large arrays—being sensilla, nanowires, or arrays of micropillars (44, 45)—will depend on their relative positions, the flow speed, and flow direction.

Materials and Methods

Natural Antennae. Cocoons of the moth *S. cynthia* were obtained from Office Pour les Insectes et leur Environnement. After emergence, moths were frozen (by placing in a freezer) and allowed to dry at room temperature for a month. Their antennae were then removed and observed in a scanning electron microscope (SEM) (Quanta 450, Field Electron and Ion Company) without metal coating.

Sensillum density and shape were observed on the SEM images obtained. Measurements were made on 12 rami from five antennae from five male moths. The rami had a diameter of 54 ± 7.0 μm (mean ± SE). We measured five sensilla at each location. The sensilla were found to be 123 ± 34 μm long for a diameter of 2.3 ± 0.79 μm. In our model, we considered ramus diameter to be equal to 50 μm, and the sensilla were considered to be 150 μm long and to have a diameter of 3 μm.

Mass Transfer Modeling. The goal of our model was to provide a solution for the concentration c_{cyl} of pheromone along a sensillum in steady flow conditions and to derive an expression for local mass transfer F_{cyl} along the sensillum (Fig. 4).

The classical mass transport equation is

$$\frac{\partial c}{\partial t} + (\vec{v}_{air}.\nabla)c = D\nabla^2 c, \qquad [10]$$

with c as the concentration of pheromone in air,

$\vec{v}_{air}$ as the velocity of air, and

D as the diffusion coefficient of the pheromone in air (all variables are shown in Table 1).

The equation is not easy to solve, given the complex geometry of the microstructure, and we resorted to an approximate semianalytical formulation. We modeled the microstructure as a 2D infinite square array of sensilla, with each sensillum modeled as a semiinfinite cylinder with a diameter equal to that of the sensilla (Fig. 1*C*). As the array was infinite, each cylinder can be considered to behave in an identical manner, and a single cylinder with appropriate boundary conditions mimicking the infinity of the array can therefore be considered. A semiinfinite cylinder can be used to model the effect of a sensillum facing the flow, and we restricted the results to a length equal to that of a natural sensillum, starting from the tip of the cylinder. We also assumed that the presence of the rest of the cylinders downstream had no marked effect on upstream flow.

Heat transfer in arrays of semiinfinite longitudinal cylinders has been investigated by Miyatake and Iwashima (15). We made use of the well-known similarity between heat and mass transfers to apply their model to our problem. Heat and mass transfers are both convective phenomena characterized by a diffusion coefficient and similar transport equations. Replacing the thermal diffusivity α and the temperature T with mass diffusivity D and pheromone concentration c, respectively, converts the heat transfer equation into the mass transfer equation. As a consequence, heat transfer results can be adapted to mass transfer problems and vice versa. The definitions of the variables are listed in Table 1, and the analogies are summarized in *SI Appendix*, Table S1. The diffusion coefficient of the pheromone was determined as described by ref. 46 (*SI Appendix*).

We also ensured that our boundary conditions were equivalent. First, the cylinders were considered to be distributed in a square array of side $2s$ (Fig. 1*C*). Second, the concentration at the surface of the sensilla c_s was assumed to be uniform and null. This is equivalent to considering a pheromone molecule reaching the surface of a sensillum to be absorbed by the surface and not released into the air again. Biologically, it is reasonable to assume a null concentration at the surface of the sensillum given the very low concentration of pheromone molecules in air: The sensillum surface is unlikely to be close to its saturation capacity. Third, the fluid was assumed to be fully laminar. Fluid flowing into the volume was considered to have a constant and uniform velocity v_n and a concentration c_∞. Fourth, the far-field concentration c_∞ was assumed spatially uniform, implying that the microstructure is reached by a filament of odor with a cross-section perpendicular to the direction of flow and larger than the frontal area of the microstructure. We set the far-field concentration at 1 $mg \cdot m^{-3}$ (47). Fifth, we considered the steady state, in which fluid flow and mass transfer are dependent on space (i.e., position along the sensilla), but remain constant over time. By definition, the cylinders modeled experience a flow that is bound to pass through the tubular array, the near flow.

Experiments. Some of the air flows around the whole microstructure, rather than through it, so the molecules it carries are out of reach of the sensilla. The reference flux F_{ref} must therefore be defined according to v_∞ and not v_n as used for the reference flux of the model (Eq. **8**). We determined the leakiness of the microstructure by PIV visualizations.

Fabrication of an artificial microstructure by additive manufacturing. An artificial microstructure was produced in black photoreactive resin (Formlabs) with a Form2 3D printer (Formlabs). It was produced scaled up by a factor of $\alpha = 300$ relative to the natural structure, for two reasons. Firstly, it needed to be large enough for flow to be measured accurately. Secondly, the sensilla needed to be thick enough to survive mechanical loading during the building process. The artificial microstructure was 13 cm long, with a ramus of 1.5-cm diameter and sensilla of 0.9-mm diameter.

PIV. We ran PIV experiments with the artificial microstructure in oil to obtain the velocity field (Fig. 3). We measured the velocity field on a cross-section in the middle of the artificial microstructure, to limit the influence of edge effects (for more details on the experimental setup, see *SI Appendix*). We used a wide range of velocities to cover the amplitude of flows through an antenna induced by wind on a resting moth, or flows occurring during a simulated moth flight. We therefore considered an air velocity span of three orders of magnitude and chose the velocities $\{0.002, 0.005, 0.1, 0.2, 0.5, 1, 2, 5\}$ $m \cdot s^{-1}$ for study. In terms of Reynolds numbers, using the sensillum diameter as the characteristic length, we obtained the following values:

$$\mathrm{Re}_{air} = \frac{d_s * v_{air}}{\nu_{air}}, \qquad [11]$$

with d_s as the sensillum diameter (3 μm),

v_{air} as the velocity of air, and

ν_{air} as the kinematic viscosity of air (15.6×10^{-6} $m^2 \cdot s^{-1}$ at 20 °C).

We changed both the velocity and the viscosity of the fluid to keep the same Reynolds number while working with an artificial microstructure two orders of magnitude larger than the natural microstructure. Instead of working in air, we ran our experiments in rapeseed oil, which has a measured kinematic viscosity of 50×10^{-6} $m^2 \cdot s^{-1}$ at 29 °C (Rolling ball viscometer: Lovis 2000, Anton Paar). The correspondence between oil and air velocities is indicated in Table 2.

Estimating leakiness. Leakiness corresponds to the proportion of molecules available to the sensilla. It is defined as the flow (velocity times area) passing through the microstructure divided by the flow passing through an identical frontal area in the absence of the microstructure (19). The frontal area is equal to the area of the microstructure projected onto a plane perpendicular to the direction of the flow. Leakiness is thus the ratio of the measured flux to the reference flux. A leakiness of zero indicates that the structure is impermeable. As the permeability of the structure increases, its leakiness increases to a maximum of 1, corresponding to a completely permeable structure, equivalent to no structure at all. However, at such low Reynolds numbers, wall effects are not negligible anymore and tend to artificially increase leakiness (48). We thus ran simulations on a simplified model of the microstructure and determined a coefficient of correction for each velocity that we applied to the leakiness obtained experimentally (*SI Appendix*). Leakiness is a relative measurement, and we worked in steady state. Leakiness can therefore be considered to be identical in dynamically scaled configurations or, in other words, in configurations with equal Reynolds numbers. We were therefore able to measure leakiness on a scaled-up microstructure in oil and apply the resulting measurements to a natural microstructure in air.

We were interested in the flow bringing molecules into the neighborhood of the sensilla. We therefore compared the flow between the most outward-facing sensilla of the microstructure (flow through the

Downloaded at UNIVERSITEIT TWENTE on November 5, 2020

Table 1. List of variables and constants used in the model

	Unit	Description	Details
Geometric parameters			
L_{ant}	1 cm	Antenna length	Measurements
d_s	3 μm	Sensillum diameter	Measurements
L_s	150 μm	Sensillum length	Measurements
α	300	Scaling factor	
d_{sart}	900 μm	Diameter of an artificial sensillum	$d_{sart} = \alpha d_s$
L_{antart}	13 cm	Length of the artificial microstructure	
s	16 μm	Half distance between sensilla	Measurements
σ	10.7	Dimensionless distance between cylinders	$\sigma = 2s/d_s$
ϕ	9.7	Dimensionless spacing between sensilla	$\phi = \sigma - 1$
$d_0 = d_s$		Diameter of the cylinder in the heat transfer model	$d_0 = d_s$
S_{front}	m^2	Frontal area	See *SI Appendix*
Experimental parameters			
v_{air}	$m \cdot s^{-1}$	Air velocity	
v_{oil}	$m \cdot s^{-1}$	Oil velocity	
v_∞	$m \cdot s^{-1}$	Far-field air velocity in the PIV experiment	
v_n	$m \cdot s^{-1}$	Mean air velocity close to the microstructure	
c_{cyl}	$g \cdot m^{-3}$	Uniform concentration at the surface of a sensillum	
c_∞	$g \cdot m^{-3}$	Far-field pheromone concentration	
Dimensionless numbers			
Le		Leakiness	Eq. **12**
Re_{air}		Reynolds number in air	Eq. **11**
Re_{oil}		Reynolds number in air	$Re_{oil} = \frac{\alpha d_s * v_{oil}}{\nu_{oil}}$
Nu		Nusselt number	See *SI Appendix*
Sh		Sherwood number	See *SI Appendix*
Gz		Graetz number	See *SI Appendix*
Physical parameters			
ν_{air}	$15.6 \times 10^{-6}\ m^2 \cdot s^{-1}$	Kinematic viscosity of air at 20 °C	
ν_{oil}	$50 \times 10^{-6}\ m^2 \cdot s^{-1}$	Kinematic viscosity of rapeseed oil at 29 °C	Measurement
D	$4.5 \times 10^{-6}\ m^2 \cdot s^{-1}$	Diffusion coefficient of pheromone	See *SI Appendix*
w_{mod}	$m^3 \cdot s^{-1}$	Volume flow rate per cylinder in the model	$w_{mod} = (4 * s^2 - \pi * (\frac{d_0}{2})^2) * v_\infty^{mod}$
w_{PIV}	$m^3 \cdot s^{-1}$	Volume flow rate per cylinder in the experiment	$w_{PIV} = (4 * s^2 - \pi * (\frac{d_0}{2})^2) * v_\infty$
Variables			
v_n	$m \cdot s^{-1}$	Mean fluid velocity at the entrance to the microstructure	
$w_{through}$	$m^3 \cdot s^{-1}$	Flux between the two outermost sensilla	
w_{ref}	$m^3 \cdot s^{-1}$	Flux for an equivalent area, taken as $F_{through}$ for a fluid at velocity v_∞	
F_{in}	$g \cdot s^{-1}$	Mass flux into the control volume described in Fig. 4	
F_{out}	$g \cdot s^{-1}$	Mass flux out of the control volume described in Fig. 4	
F_{cyl}	$g \cdot m^{-1} \cdot s^{-1}$	Local mass flux to a sensillum surface in Fig. 4	
c	$g \cdot m^{-3}$	Pheromone concentration in the fluid	
c_f	$g \cdot m^{-3}$	Mean pheromone concentration in the fluid between the sensilla depending on z	
η_s		Capture efficiency of the model	
η_m		Capture efficiency of the microstructure	

microstructure) and the far-field flow through an equal area (the reference flux) (Fig. 3). This resulted in the following expression of leakiness:

$$\mathrm{Le} = \frac{w_{through}}{w_{ref}}, \quad [12]$$

with $w_{through}$ as the flow between the two outermost sensilla of the microstructure and

w_{ref} as the reference flow.

Further calculations (*SI Appendix*) showed that

$$\mathrm{Le} = \frac{v_n}{v_\infty}, \quad [13]$$

or, equivalently,

$$v_n = \mathrm{Le} * v_\infty. \quad [14]$$

Combining the Model and the PIV Experiment. The model provides expressions for both the capture efficiency of a sensillum, $\eta_s(v_n)$, and the mass flux on a sensillum, $F_s(v_n)$, depending on v_n. The PIV experiment

Table 2. Experimental Reynolds numbers and relative velocities in air and oil

	Reynolds number							
	0.004	0.01	0.02	0.04	0.1	0.2	0.4	1
Air velocity $m \cdot s^{-1}$	0.02	0.05	0.1	0.2	0.5	1	2	5
Experimental oil velocity $mm \cdot s^{-1}$	0.21	0.53	1.07	2.14	5.34	10.7	21.4	53.4

Reynolds numbers in water and oil were set to equal values for determination of the oil velocity corresponding to each air velocity that we wanted to investigate.

ECOLOGY
ENGINEERING

Downloaded at UNIVERSITEIT TWENTE on November 5, 2020

provided information about leakiness, that is, the relationship between the far-field velocity v_∞ and the velocity at the entrance to the microstructure, $v_n(v_\infty)$. By combining modeling and experimental results, it is possible to express the capture efficiency of a sensillum according to far-field velocity v_∞, $\eta_s(v_\infty)$. We did the same for the mass flux on a sensillum $F_s(v_\infty)$. Thus, given Eq. **14**, we hereafter express all values of the model according to v_∞.

For determination of the capture efficiency of a microstructure η_m, we had to take into account its leakiness, which decreases the velocity from v_∞ to v_n. The easiest way to determine efficiency is to return to the mass flux on a sensilla $F_s(v_\infty)$ and define a new reference mass flux F_{ref} depending on v_∞.

$$F_{ref} = wc_\infty = 4s^2 v_\infty c_\infty. \quad [15]$$

The capture efficiency of the microstructure η_m is defined as

$$\eta_m(v_\infty) = \frac{F_s(v_\infty)}{F_{ref}(v_\infty)}. \quad [16]$$

By multiplying the numerator and denominator by $F_{ref}^{mod}(v_\infty)$ and using the expressions of the reference flows (Eqs. **8** and **15**), we obtained

$$\eta_m(v_\infty) = \frac{F_s(v_\infty)}{F_{ref}^{mod}(v_\infty)} \frac{v_n 4s^2}{v_\infty 4s^2}. \quad [17]$$

According to Eqs. **9**, **13**, and **14**, we obtained

$$\eta_m(v_\infty) = \eta_s(v_\infty)\mathrm{Le}(v_\infty). \quad [18]$$

Data Availability. Template for artificial microstructure, Comsol code, Matlab code, and raw PIV data are available on Figshare under the name Microstructure_data (https://doi.org/10.6084/m9.figshare.12631340.v1) (49).

ACKNOWLEDGMENTS. We thank the two anonymous reviewers for their comments which greatly improved the quality of this article. We thank Magaly Caravanier and Bénédicte Montigny for their help determining the rapeseed oil viscosity, Josh Loessberg-Zahl for 3D printing our artificial microstructure, and Jean-François Dufrêche for the formula about the diffusion coefficient. We acknowledge the Centre Val de Loire region for providing PhD funding for M.J.-B. and the PHEROAERO (Pheromone Capture by Aerosols) grant.

1. C. Gadenne, R. B. Barrozo, S. Anton, Plasticity in insect olfaction: To smell or not to smell? *Annu. Rev. Entomol.* **61**, 317–333 (2016).
2. J. D. Allison, R. T. Cardé, *Pheromone Communication in Moths: Evolution, Behavior, and Application* (University of California Press, Oakland, CA, 2016).
3. S. P. Foster, K. G. Anderson, J. Casas, The dynamics of pheromone gland synthesis and release: A paradigm shift for understanding sex pheromone quantity in female moths. *J. Chem. Ecol.* **44**, 525–533 (2018).
4. C. Wall, J. N. Perry, Range of action of moth sex-attractant sources. *Entomol. Exp. Appl.* **44**, 5–14 (1987).
5. M. R. E. Symonds, T. L. Johnson, M. A. Elgar, Pheromone production, male abundance, body size, and the evolution of elaborate antennae in moths. *Ecol. Evol.* **2**, 227–246 (2011).
6. P. D. N. Hebert, Egg dispersal patterns and adult feeding behaviour in the Lepidoptera. *Can. Entomol.* **115**, 1477–1481 (1983).
7. T. Tammaru, E. Haukioja, Capital breeders and income breeders among Lepidoptera: Consequences to population dynamics. *Oikos* **77**, 561–564 (1996).
8. J. A. Riffell, H. Lei, J. G. Hildebrand, Neural correlates of behavior in the moth *Manduca sexta* in response to complex odors. *Proc. Natl. Acad. Sci. U.S.A.* **106**, 19219–19226 (2009).
9. N. F. Brito, M. F. Moreira, A. C. A. Melo, A look inside odorant-binding proteins in insect chemoreception. *J. Insect Physiol.* **95**, 51–65 (2016).
10. R. A. Steinbrecht, Der Feinbau olfaktorischer Sensillen des Seidenspinners (Insecta, Lepidoptera). *Zeitschrift für Zellforschung* **139**, 533–565 (1973).
11. A. Y. L. Cheer, M. A. R. Koehl, Fluid flow through filtering appendages of insects. *J. Math. Applied Med. Biol.* **4**, 185–199 (1987).
12. J. A. C. Humphrey, H. Haj-Hariri, "Stagnation point flow analysis of odorant detection by permeable moth antennae" in *Frontiers in Sensing*, F. G. Barth, J. A. C. Humphrey, M. V. Srinivasan, Eds. (Springer, Vienna, Austria, 2012), pp. 171–192.
13. M. Jaffar-Bandjee, J. Casas, G. J. M. Krijnen, Additive manufacturing: State of the art and potential for insect science. *Curr. Opin. Insect Sci.* **30**, 79–85 (2018).
14. S. Kanaujia, K.-E. Kaissling, Interactions of pheromone with moth antennae: Adsorption, desorption and transport. *J. Insect Physiol.* **31**, 71–81 (1985).
15. O. Miyatake, H. Iwashita, Laminar-flow heat transfer to a fluid flowing axially between cylinders with a uniform surface temperature. *Int. J. Heat Mass Tran.* **33**, 417–425 (1990).
16. T. Alam, Y. Zhao, P. S. Takhar, Water and oil permeability of poroelastic potato discs. *Int. J. Food Prop.* **20**, 633–644 (2017).
17. A. A. Gubaidullin, A. S. Gubkin, D. E. Igoshin, P. A. Ignatev, Permeability of model porous medium formed by random discs*AIP Conf. Proc.* **1939**, 020035 (2018).
18. C. Strickland *et al.*, Three-dimensional low Reynolds number flows near biological filtering and protective layers. *Fluids* **2**, 1–24 (2017).
19. A. Y. L. Cheer, M. A. R. Koehl, Paddles and rakes: Fluid flow through bristled appendages of small organisms. *J. Theor. Biol.* **129**, 17–39 (1987).
20. S. Vogel, How much air passes through a silkmoth's antenna? *J. Insect Physiol.* **29**, 597–602 (1983).
21. M. Jaffar-Bandjee, T. Steinmann, G. J. M. Krijnen, J. Casas, Leakiness and flow capture ratio of insect pectinate antennae. *J. R. Soc. Interface* **17**, 20190779 (2020).
22. J. G. Swallow, G. S. Wilkinson, J. H. Marden, Aerial performance of stalk-eyed flies that differ in eye span. *J. Comp. Physiol. B* **170**, 481–487 (2000).
23. R. J. Knell, J. C. Pomfret, J. L. Tomkins, The limits of elaboration: Curved allometries reveal the constraints on mandible size in stag beetles. *Proc. Royal Soc. B* **271**, 523–528 (2004).
24. L. D. Waldrop, Y. He, S. Khatri, What can computational modeling tell us about the diversity of odor-capture structures in the Pancrustacea? *J. Chem. Ecol.* **44**, 1084–1100 (2018).
25. J. Boeckh, K.-E. Kaissling, D. Schneider, Sensillen und Bau der Antennengeißel von Telea polyphemus. *Zool. Jahrb. Abt. Anat. Ontog. Tiere* **78**, 559–584 (1960).
26. D. Schneider, K.-E. Kaissling, Der Bau der Antenne des Seidenspinners Bombyx mori L. III. Das Bindegewebe und das Blutgefäß. *Zool. Jahrb. Abt. Anat. Ontog. Tiere* **77**, 111–132 (1959).
27. R. A. Steinbrecht, Zur morphometrie der antenne des seidenspinners, Bombyx mori L.: Zahl und Verteilung der Riechsensillen (Insecta, Lepidoptera). *Zeitschrift Morphologie Tiere* **68**, 93–126 (1970).
28. T. C. Baker, R. G. Vogt, Measured behavioural latency in response to sex-pheromone loss in the large silk moth *Antheraea polyphemus*. *J. Exp. Biol.* **137**, 29–38 (1988).
29. J. R. Barber *et al.*, Moth tails divert bat attack: Evolution of acoustic deflection. *Proc. Natl. Acad. Sci. U.S.A.* **112**, 2812–2816 (2015).
30. C. Loudon, E. C. Davis, Divergence of streamlines approaching a pectinate insect antenna: Consequences for chemoreception. *J. Chem. Ecol.* **31**, 1–13 (2005).
31. J. D. Murray. "Reduction of dimensionability in diffusion processes: Antenna receptors of moths" in *Nonlinear Differential Equation Models in Biology* (Oxford University Press, Oxford, United Kingdom, 1977), pp. 83–127.
32. M. Jaffar-Bandjee, G. J. M. Krijnen, J. Casas, Challenges in modeling pheromone capture by pectinate antennae. *Integr. Comp. Biol.*, icaa057 (2020).
33. Q. Wang *et al.*, Antennal scales improve signal detection efficiency in moths. *Proc. Royal Soc. B* **285**, 20172832 (2018).
34. T. L. Spencer *et al.*, Moth-inspired methods for particle capture on a cylinder. *J. Fluid Mech.* **884**, A34 (2020).
35. R. C. Schuech, M. T. Stacey, M. F. Barad, M. A. R. Koehl, Numerical simulations of odorant detection by biologically inspired sensor arrays. *Bioinspir. Biomim.* **7**, 016001 (2012).
36. L. Conchou *et al.*, Insect odorscapes: From plant volatiles to natural olfactory scenes. *Front. Physiol.* **10**, 972 (2019).
37. A. Mafra-Neto, R. T. Cardé, Fine-scale structure of pheromone plumes modulates upwind orientation of flying moths. *Nature* **369**, 142–144 (1994).
38. K.-E. Kaissling, "The sensivity of the insect nose: The example of *Bombyx mori*" in *Biologically Inspired Signal Processing for Chemical Sensing*, A. Gutiérrez, S. Marco, Eds. (Springer, Berlin, Germany, 2009), pp. 45–52.
39. K.-E. Kaissling, "Pheromone reception in insects: The example of silk moths" in *Neurobiology of Chemical Communication*, C. Mucignat-Caretta, Eds. (CRC Press, 2014), pp 99–146.
40. M. M. Maitani, D. L. Allara, K. C. Park, S. G. Lee, T. C. Baker, Moth olfactory trichoid sensilla exhibit nanoscale-level heterogeneity in surface lipid properties. *Arthropod Struct. Dev.* **39**, 1–16 (2010).
41. M. A. Elgar *et al.*, Insect antennal morphology: The evolution of diverse solutions to odorant perception. *Yale J. Biol. Med.* **91**, 457–469 (2018).
42. S. K. Vashist, J. H. Luong, "Microcantilever-based sensors" in *Handbook of Immunoassay Technologies*, S. K. Vashist, J. H. Luong, Eds. (Academic, 2018), pp. 305–332.
43. E. Sage *et al.*, Single-particle mass spectrometry with arrays of frequency-addressed nanomechanical resonators. *Nat. Commun.* **9**, 3283 (2018).
44. J. Casas, T. Steinmann, G. J. M. Krijnen, Why do insects have such a high density of flow-sensing hairs? Insights from the hydromechanics of biomimetic MEMS sensors. *J. R. Soc. Interface* **7**, 1487–1495 (2010).
45. G. J. M. Krijnen, T. Steinmann, R. K. Jaganatharaja, J. Casas, "Insect-inspired distributed flow-sensing: Fluid-mediated coupling between sensors" in *Architectured Materials in Nature and Engineering*, Y. Estrin, Y. Bréchet, J. Dunlop, P. Fratzl, Eds. (Springer, Cham, Switzerland, 2019), pp. 355–392.
46. M. J. Tang, M. Shiraiwa, U. Pöschl, R. A. Cox, M. Kalberer, Compilation and evaluation of gas phase diffusion coefficients of reactive trace gases in the atmosphere: Volume 2. Diffusivities of organic compounds, pressure-normalised mean free paths, and average Knudsen numbers for gas uptake calculations. *Atmos. Chem. Phys.* **15**, 5585–5598 (2015).
47. L. L. Stelinski, L. J. Gut, J. R. Miller, Concentration of air-borne pheromone required for long-lasting peripheral adaptation in the obliquebanded leafroller, *Choristoneura rosaceana*. *Physiol. Entomol.* **28**, 97–107 (2003).
48. C. Loudon, B. A. Best, M. A. R. Koehl, When does motion relative to neighboring surfaces alter the flow through arrays of hairs? *J. Exp. Biol.* **193**, 233–254 (1994).
49. M. Jaffar-Bandjee, Microstructure_data. Figshare. https://doi.org/10.6084/m9.figshare.12631340.v1. Deposited 7 September 2020.

Downloaded at UNIVERSITEIT TWENTE on November 5, 2020